Efficient fixed point and Newton–Krylov solvers for FFT-based homogenization of elasticity at large deformations

Matthias Kabel, Thomas Böhlke, Matti Schneider

To cite this version:

Matthias Kabel, Thomas Böhlke, Matti Schneider. Efficient fixed point and Newton–Krylov solvers for FFT-based homogenization of elasticity at large deformations. Computational Mechanics, 2014, 54 (6), pp.1497-1514. 10.1007/s00466-014-1071-8 . hal-03651746

Efficient fixed point and Newton–Krylov solvers for FFT-based homogenization of elasticity at large deformations

Matthias Kabel · Thomas Böhlke · Matti Schneider

Abstract In recent years the FFT-based homogenization method of Moulinec and Suquet has been established as a fast, accurate and robust tool for obtaining effective properties in linear elasticity and conductivity problems. In this work we discuss FFT-based homogenization for elastic problems at large deformations, with a focus on the following improvements. Firstly, we exhibit the fixed point method introduced by Moulinec and Suquet for small deformations as a gradient descent method. Secondly, we propose a Newton–Krylov method for large deformations. We give an example for which this methods needs approximately 20 times less iterations than Newton's method using linear fixed point solvers and roughly 100 times less iterations than the nonlinear fixed point method. However, the Newton–Krylov method requires 4 times more storage than the nonlinear fixed point scheme. Exploiting the special structure we introduce a memory-efficient version with 40 % memory saving. Thirdly, we give an analytical solution for the micromechanical solution field of a two-phase isotropic St.Venant–Kirchhoff laminate. We use this solution for comparison and validation, but it is of independent interest. As an example for a microstructure relevant in engineering we discuss finally the application of the FFT-based method to glass fiber reinforced polymer structures.

Keywords Composite materials · Finite deformations · Lippmann–Schwinger equation · FFT

Mathematics Subject Classification 74B20 · 45G10 · 65T50

1 Introduction

The macroscopic constitutive behavior of applied materials is governed by both the microstructure and the material behavior of the phases. Prominent examples are polycrystalline metals, fiber reinforced polymers and high-strength ceramics. Modern experimental techniques, for example microtomography or electron back-scattering diffraction, allow for the determination of microstructures for all of these materials.

Nonlinear continuum mechanical theories have the potential to describe the bulk behavior of the phases as well as the response of the interfaces. The determination of micro- or mesoscopic mechanical field quantities, e.g. stresses and strains, for given macroscopic quantities is called localization, the estimate of effective properties based on the local continuum mechanical fields is called homogenization [11,34]. Localization and homogenization techniques are necessary in order to understand complex material behavior based on virtual experiments and to optimize and to design new materials and components [15,41,42].

This work was conducted while MK enjoyed a sabbatical leave at the Karlruhe Institute of Technology (KIT). MS gratefully acknowledges financial support by the German Research Foundation (DFG), Federal Cluster of Excellence EXC 1075 "MERGE Technologies for Multifunctional Lightweight Structures".

M. Kabel (✉)
Department of Flow and Material Simulation, Fraunhofer ITWM,
Kaiserslautern, Germany
e-mail: matthias.kabel@itwm.fraunhofer.de

T. Böhlke
Intitute of Engineering Mechanics, Karlruhe Institute
of Technology, Karlsruhe, Germany
e-mail: thomas.boehlke@kit.edu

M. Schneider
Faculty of Mechanical Engineering , Chemnitz University
of Technology, Chemnitz, Germany
e-mail: matti.schneider@mb.tu-chemnitz.de

The application of simulation techniques in the context of large deformations is necessary since almost no exact solutions are available. Examples where geometrically nonlinear deformation processes have to be considered are deformation induced crystallographic textures in metals [21] and semicrystalline polymers [2]. The proper description of large deformations requires a geometrically as well as a physically nonlinear constitutive modeling.

The FFT-based homogenization method was proposed by Moulinec and Suquet in the middle of the 1990s [30] for problems of linearized elasticity based on the Lippmann–Schwinger equation in elasticity [24,47]. Since no meshing is required and the assembly of the linear system is avoided, the memory needed for solving the problem is significantly reduced compared with other methods.

Accelerated linear solvers have been proposed by Eyre and Milton [14] based on an ingenious rewriting of the Lippmann–Schwinger equation, by Michel, Moulinec and Suquet [26] exploiting the augmented Lagrangian method (see also [28]), and, most recently, by Zeman et al. [48] and Brisard and Dormieux [8] making use of Krylov subspace solvers. See [32] for a numerical comparison.

Moulinec and Suquet extended their fixed-point method to nonlinear problems at small strains [31]. Similarly, Vinogradov and Milton [44] combined the Newton–Raphson [35,36] with the Moulinec–Suquet method to tackle problems of nonlinear thermoelasticity (compare [29] for a direct application of the Eyre–Milton method to nonlinear problems). Gélébart and Mondon–Cancel [17] introduced the idea of applying Krylov solvers to the linear problems of the Newton–Raphson procedure at small strains.

For large deformations Lahellec, Moulinec, and Suquet [25] proposed to solve the nonlinear Lippmann–Schwinger equation for finite strains by the Newton–Raphson method and the linear Moulinec–Suquet fixed point solver. In contrast, Eisenlohr et al. [13] suggested using the Moulinec–Suquet fixed point iteration on the nonlinear Lippmann–Schwinger equation for finite strains directly.

The present work has three core themes. Firstly, we clarify the origin of the linear and nonlinear fixed point solver of Moulinec and Suquet. Quite naturally it arises as a gradient descent method applied to the (hyper) elastic energy. This geometric reinterpretation sheds new light on the convergence behavior of the method, choice of parameters, and limitations in convergence speed. For instance, restrictions on the reference material directly correspond to stability conditions for the gradient descent method. Secondly, we propose to carry over the ideas of Vinogradov and Milton [44] and of Gélébart and Mondon–Cancel [17] of combining the Newton–Raphson procedure with fast linear solvers to the geometrically nonlinear case. Apparently elastic problems with large deformations favour Krylov subspace solvers. This is due to an instability phenomenon of the linear fixed point solvers not present at small deformations. The Newton–Krylov method is extremely fast, but requires excessive memory. For instance on a 512^3 voxel image the basic fixed point iteration of Moulinec and Suquet uses 9 GBs of memory, the Newton–Eyre–Milton methods needs 18 GBs of memory, whereas the Newton–Krylov method requires 45 GBs of memory. We propose a modification of the Newton–Krylov method that exploits the special structure of the Krylov iterates and Green's operator, but fully preserves the convergence speed, reducing the memory requirements by 40 %. For the example above we only need 27 GBs of memory, and we provide a numerical example where our method is 100 times faster than the nonlinear fixed point iteration. Furthermore, we introduce a memory-efficient convergence criterion for the linear and nonlinear fixed point solvers. Using the criteria suggested in the literature doubles the memory requirement of the fixed point solvers. Thirdly, we introduce an analytical solution for a rank-one laminate consisting of two St.Venant–Kirchhoff materials. This class of materials is particularly simple and can correctly describe small strain—large deformation behavior. To the best of our knowledge, this explicit solution is not mentioned in the literature. We use the laminate solution for comparison and accuracy tests of the FFT-based solvers, we consider the solution to be of immanent independent interest, however. For a particular choice of elastic parameters, a bifurcation occurs for a particular intensity of compression which is not present for elongation. From a mechanical perspective we see that the effective behavior cannot be adequately described by a St.Venant–Kirchhoff material, which is quite interesting. From the numerical viewpoint this bifurcation poses severe challenges to any numerical solver, constituting a brilliant test case. The numerical examples in this article were implemented and tested with the commercial code FeelMath,[1] distributed as part of GeoDict.[2]

This article is organized as follows. Section 2 is devoted to the reformulation of the elastostatic problem at finite strains in terms of an equivalent integral equation of Lippmann–Schwinger type. Section 3 contains algorithms of the studied FFT-based methods for large strains, a reformulation of the basic scheme as a gradient descent method, a discussion of the instability of linear fixed point solvers, and of the problem of indefinite tangential stiffness. In Sect. 4 we consider a rank-one laminate that consists of two materials of St.Venant–Kirchhoff type [12] and derive a set of implicit analytic solutions for the deformation at finite strains. Finally, in Sect. 5 we show that the FFT-based methods reproduce the mechanical fields in the rank-one laminate even if multiple solutions exist and compare the computational costs of the different FFT-based schemes. Afterwards we apply the

---

[1] www.itwm.fraunhofer.de/FeelMath

[2] www.geodict.com/ElastoDict

FFT-based methods to a microstructure typical for glass fiber reinforced plastics (GFRP).

2 The Lippmann–Schwinger equation in hyperelasticity

Let $d \in \mathbb{N}_+$, $L_i > 0$ for $i = 1, \ldots, d$. In a Lagrangian setting with periodic boundary conditions the (static) equilibrium condition for the representative element $\mathbb{T}^d = \mathbb{R}/L_1\mathbb{Z} \times \cdots \times \mathbb{R}/L_d\mathbb{Z}$ without volume forces is given by [40,43]

$$\operatorname{Div}(P) = 0 \tag{1}$$

with the 1st-Piola–Kirchhoff stress tensor $P = FS$, $F = \bar{F} + \nabla u$ and u being the periodic fluctuation field, i.e.

$$u(x_1, \ldots, x_i + L_i, \ldots, x_d) = u(x_1, \ldots, x_d), \tag{2}$$

for $i = 1, \ldots, d$. The operator $\operatorname{Div}(\cdot)$ represents the divergence operator in the reference configuration of the body. Combining a constitutive equation for the 2nd-Piola–Kirchhoff stress tensor $S = \det(F)F^{-1}\sigma F^{-T}$ with the equilibrium condition (1) gives a set of explicit field equations for the determination of the periodic fluctuation field which depend on the prescribed average deformation gradient $\bar{F}$.

Let $\mathbb{C}^0$ be a constant reference stiffness satisfying

$$F : \mathbb{C}^0 : F \geq c\, F : F, \quad \forall F \in \mathbb{R}^{3\times 3}, \tag{3}$$

for a positive constant c independent of F. Introducing the stress polarization

$$\tau = P(F) - \mathbb{C}^0 : F, \tag{4}$$

the equilibrium Eq. (1) transforms into the relation

$$\operatorname{Div}(\mathbb{C}^0 : \nabla u) = -\operatorname{Div}(\tau). \tag{5}$$

Denote by $G^0 : [H_\#^{-1}(\mathbb{T}^d)]^d \to [H_\#^1(\mathbb{T}^d)]^d$ the solution operator of the linear reference problem, which associates to a right-hand side f the solution u of the variational equation

$$\int_{\mathbb{T}^d} \nabla v : \mathbb{C}^0 : \nabla u \, dX = -\int_{\mathbb{T}^d} f \cdot v \, dX, \forall v \in [H_\#^1(\mathbb{T}^d)]^d. \tag{6}$$

The subscript # denotes function spaces with vanishing mean value. Then

$$\nabla u = -\nabla G^0 \operatorname{Div}(\tau) = -\nabla G^0 \operatorname{Div}(P(F) - \mathbb{C}^0 : F) \tag{7}$$

or, equivalently,

$$F = \bar{F} - \Gamma^0 : (P(F) - \mathbb{C}^0 : F), \tag{8}$$

with

$$\Gamma^0 = \nabla G^0 \operatorname{Div}. \tag{9}$$

The Lippmann–Schwinger Eq. (8) was first introduced in [23,47] and is equivalent to the variational form

$$\int_{\mathbb{T}^d} \nabla v : P(\bar{F} + \nabla u)\, dX = 0, \quad \forall v \in [H_\#^1(\mathbb{T}^d)]^d, \tag{10}$$

of the equilibrium Eq. (1) (the proof of [46] for small deformations carries over directly). The bounded linear operator $\Gamma^0 : [L^2(\mathbb{T}^d)]^{d\times d} \to [L^2(\mathbb{T}^d)]^{d\times d}$ is usually called Green's operator.

In contrast to [13] and in accord with [10] we do not use linear elasticity as our reference problem. Indeed, since a linearly elastic $\mathbb{C}^0$ satisfies minor symmetries, it necessarily violates (3). This inequality, however, serves as the basis to prove rigorous error bounds for the linear systems arising in the Newton–Raphson iterations, cf. the bounds (28), (34), and (36).

3 FFT-based schemes

Following [30,31] we discretize the nonlinear Lippmann–Schwinger Eq. (8) by the method of trigonometric collocation, see [5,39] for background material.

There are basically two solution strategies to solve (8). Firstly, one can use a fixed point iteration on the nonlinear equation, introduced in [31] for small deformations and extended to large deformations in [13]. Alternatively, one can use the Newton–Raphson method [35,36] to tackle the nonlinear problem by solving a sequence of linear problems. These linear problems can either be solved by the fixed point method of Moulinec and Suquet [25,30,31], the fixed point method of Eyre and Milton [14] or Krylov subspace solvers [8,9,48] (see also [17] for small deformations). Although all these algorithms directly iterate on deformation gradient fields and do not compute the corresponding displacement fields, their iterates satisfy compatibility due to Eq. (9).

In this section, we exhibit the fixed point scheme of Moulinec and Suquet as a gradient descent method, explaining its basic mechanisms. Furthermore, we propose memory-minimal variants of all algorithms, including convergence criteria, and discuss the choice of reference material ensuring fastest convergence. For instance, our Newton–Krylov (conjugate gradient) method requires 40 % less memory than a naive implementation, and has identical iterates.

3.1 Basic scheme

Moulinec and Suquet [30,31] proposed to use the fixed point form of Eq. (8) as the basis of an algorithm, and to compute the action of Γ^0 efficiently by fast Fourier transform (FFT). More precisely, they proposed the Algorithm 1, where the basic Moulinec–Suquet iteration is performed in place. Algorithm 1 is easily extended to incorporate multiple load steps $\{\bar{F}_n\}$, compare Algorithm 2. An explicit formula for the Fourier coefficients $\hat{\Gamma}^0$ of Green's operator can be found in the Appendix 7.

Algorithm 1 Basic scheme [31]

```
$F \leftarrow \bar{F}$                    ▷ $\bar{F}$ is the prescribed macroscopic load
repeat
    $F \leftarrow$ MSiterate($F$,$P$,$\mathbb{C}^0$,$\bar{F}$)
until Convergence
return $F$
MSiterate($F$,$P$,$\mathbb{C}^0$,$\bar{F}$)
$F \leftarrow P(F) - \mathbb{C}^0 : F$
$F \leftarrow$ FFT($F$)
$F \leftarrow -\hat{\Gamma}^0 : F, \quad F(0) = \bar{F}$
$F \leftarrow$ FFT$^{-1}$($F$)
return $F$
```

Algorithm 2 Basic scheme (multiple load steps)

```
$F \leftarrow \bar{F}_0$
for $n \in \{0, \dots, n_{\max}\}$ do
    repeat
        $F \leftarrow$ MSiterate($F$,$P$,$\mathbb{C}^0$,$\bar{F}_n$)
    until Convergence.
end for
return F
```

To understand the basic scheme we will reformulate it as a gradient descent method. First recall the notion of gradient from Riemannian geometry. Let M be a manifold, endowed with a Riemannian metric g, i.e. a family $(g_x)_{x\in M}$ of inner products on the tangent spaces $(T_x M)_{x\in M}$. The gradient of a continuously differentiable function $f : M \to \mathbb{R}$ is defined by the equality

$$g(\mathrm{GRAD} f(x), \xi) = Df(x)[\xi], \quad x \in M, \xi \in T_x M, \tag{11}$$

where $Df(x)[\xi]$ denotes the derivative of f at x in direction ξ. The space

$$V = \left\{ G \in [L^2(\mathbb{T}^d)]^{d\times d} \,\middle|\, \exists u \in [H^1_\#(\mathbb{T}^d)]^d : G = \nabla u \right\} \tag{12}$$

is a closed subspace of $[L^2(\mathbb{T}^d)]^{d\times d}$. For fixed $\bar{F} \in \mathbb{R}^{d\times d}$ the space

$$M = \left\{ \bar{F} + G \in [L^2(\mathbb{T}^d)]^{d\times d} \,\middle|\, G \in V \right\} \tag{13}$$

is an affine manifold modelled on the Hilbert space V. In particular, the tangent space $T_F M$ at $F \in M$ can be identified with V. We endow M with the Riemannian metric

$$g(G, H) = \int_{\mathbb{T}^d} G : \mathbb{C}^0 : H \, dX, \quad G, H \in V, \tag{14}$$

for some fixed reference tensor $\mathbb{C}^0$ satisfying (3). Suppose that we have a hyperelastic energy density function $\overline{W} : \mathbb{T}^d \times \mathbb{R}^{d\times d} \to \mathbb{R}$, i.e. $D\overline{W}(F) = P(F)$, where D refers to the derivative in the second variable only. In particular, solutions of the equilibrium condition (1) correspond to critical points of the total hyperelastic energy

$$f(F) = \int_{\mathbb{T}^d} \overline{W}(F) \, dX, \quad F \in M, \tag{15}$$

where we consistently suppress the X-dependence. Then Eq. (11) reads

$$g(\mathrm{GRAD} f(F), G) = Df(F)[G], \quad F \in M, G \in V. \tag{16}$$

Writing $G = \nabla v$ for some v the right hand side of (16) becomes

$$\int_{\mathbb{T}^d} P(F) : \nabla v \, dX, \tag{17}$$

whereas the left hand side reads

$$\int_{\mathbb{T}^d} \mathrm{GRAD} f(F) : \mathbb{C}^0 : \nabla v \, dX. \tag{18}$$

Writing $\mathrm{GRAD} f(F) = \nabla u$ for $u \in [H^1_\#(\mathbb{T}^d)]^d$ we see that u solves the variational equation

$$\int_{\mathbb{T}^d} \nabla u : \mathbb{C}^0 : \nabla v \, dX = \int_{\mathbb{T}^d} P(F) : \nabla v \, dX, \quad v \in [H^1_\#(\mathbb{T}^d)]^d, \tag{19}$$

i.e.

$$u = G^0 \mathrm{Div} P(F), \tag{20}$$

$$\mathrm{GRAD} f(F) = \nabla u = \Gamma^0 : P(F). \tag{21}$$

Suppose we have a family F_t of solutions to the gradient descent equation

$$\frac{dF_t}{dt} = -\mathrm{GRAD} f(F_t). \tag{22}$$

Then,

$$\begin{aligned}\frac{d}{dt}f(F_t) &= Df(F_t)\left[\frac{dF_t}{dt}\right]\\ &= g(\mathrm{GRAD}f(F_t), -\mathrm{GRAD}f(F_t))\\ &= -\int_{\mathbb{T}^d}(\Gamma^0 : P(F_t)) : \mathbb{C}^0 : (\Gamma^0 : P(F_t))\,dX\\ &\leq -C\|\mathrm{Div}P(F_t)\|^2_{H^{-1}} \qquad (23)\end{aligned}$$

for a constant depending only on $\mathbb{C}^0$. In particular, the hyperelastic energy decreases monotonically as long as $\mathrm{Div}P(F_t) \neq 0$. A forward Euler discretization of the gradient descent method (22) with time step Δt and initial guess F^0 reads

$$\begin{aligned}F^{i+1} &= F^i - \Delta t\mathrm{GRAD}f(F^i)\\ &= F^i - \Delta t\mathrm{GRAD}f(F^i)\\ &= F^i - \Delta t\Gamma^0 : P(F^i)\\ &= (1-\Delta t)F^i + \Delta t(\bar{F} - \Gamma^0 : (P(F^i) - \mathbb{C}^0 : F^i)).\end{aligned} \qquad (24)$$

Here, we have used the equality $F = \bar{F} + \Gamma^0 : \mathbb{C}^0 : F$ for $F \in M$. We see that the gradient descent with $\Delta t = 1$ corresponds directly to the basic scheme. $\Delta t < 1$ leads to a relaxed formulation, sometimes called damped Picard iteration. This reformulation has several important consequences.

1. Under mild hypotheses on the hyperelastic energy, like some coercivity assumption, and sufficiently small time steps we see that the basic scheme converges to a critical point.
2. The chosen reference material determines the Riemannian metric, directly influencing the descent direction. However, it is not necessary to choose a truly anisotropic reference material like Eisenlohr et al. [13].
3. The convergence speed of the method is limited. One should compare to the linear case, where CG converges significantly faster compared to a pure gradient descent [48].
4. Assuming sufficiently small time steps (or large iteration number) the hyperelastic energy decreases monotonically. Thus, the related hyperelastic energy difference can be used as an inexpensive stopping criterion.
5. These conclusions remain valid for small deformations.

The choice of reference stiffness is central to the convergence speed of the basic scheme. Suppose we have an initial guess $\mathbb{C}^0$ and scale with a positive factor $\varepsilon > 0$. Then, the corresponding gradient scales as $\varepsilon^{-1}\mathrm{GRAD}f(F)$. If ε is very small, the gradient becomes prohibitively large, leading to an unstable method. Large ε, on the other hand, slows down the method significantly.

The choice of reference material for the nonlinear basic scheme is not discussed in the literature to the best of the authors' knowledge, with the notable exception of Eisenlohr et al. [13]. They propose to determine $\mathbb{C}^0$ as the mean value of dP/dF in the current configuration.

In this work we propose to use as reference material a scalar multiple of the identity on $d \times d$ matrices. The scalar factor in front of the identity is computed as the average of the maximal and minimal (positive) eigenvalue of dP/dF in the current configuration. This choice can be proved to be theoretically optimal for anisotropic linear elasticity and is simple to implement. Our choice has the following advantages in comparison to [13].

1. In general the averaging approach of [13] leads to fully anisotropic reference materials. These do not admit explicit formulae for the Green's operator. Thus in three spatial dimensions one either has to invert a (symmetric) 9×9 matrix for every voxel and every Moulinec–Suquet iteration or compute these once and store them, requiring the equivalent of 9 deformation gradients. Furthermore, the averaged reference material [13] need not be positive. In contrast, we can make make use of explicit formulas for the Fourier coefficients of the Green's operator (cf. Appendix 7), and our $\mathbb{C}^0$ is always positive definite.
2. It is possible to construct examples for which the choice of the average of the elastic stiffness as reference material is detrimental for the convergence behavior. For simplicity, we have chosen an example in linear elasticity. Consider a two-phase laminate consisting of isotropic linear elastic materials $\mathbb{C}^1 = 2\mu_1\mathbb{I}^S$ and $C^2 = 2\mu_2\mathbb{I}^S$ with $\mathbb{I}^S$ being the identity tensor on 2nd-order symmetric tensors. The (theoretically) optimal reference material is defined by $\mathbb{C}^0 = (\mu_1 + \mu_2)\mathbb{I}^S$ [26], whereas volume averaging gives $\mathbb{C}^0 = 2(c_1\mu_1 + c_2\mu_2)\mathbb{I}^S$ with c_1 and c_2 denoting the volume fractions of the two phases. For $c_1 \to 0$ or $c_1 \to 1$ the difference of the two reference materials becomes large for high material contrasts μ_1/μ_2. For $\mu_1 = 500$ [GPa] and $\mu_2 = 0.5$ [GPa] we can actually choose the volume fractions in such a way that the volume average of the stiffness leads to divergence of the basic scheme (see Table 1, – indicates divergence).

Similarly, a clever choice of the convergence criterion can reduce the computational costs. In contrast to other authors [8,28,31] who suggested criteria that need storage for both the deformation gradient and the first Piola–Kirchhoff stress, we propose to use a less memory and time consuming convergence test for the basic scheme that only needs the L^2-norm of the iterates

Table 1 Deformation of a linear elastic two-phase laminate

c_1 [−]	$\mu^0 = c_1\mu_1 + c_2\mu_2$ [GPa]	# Iter. [−]	$\mu^0 = (\mu_1 + \mu_2)/2$ [GPa]	# Iter. [−]
0.1	50.45	–	250.25	48
0.2	100.40	–	250.25	23
0.3	150.35	–	250.25	13
0.4	200.30	18	250.25	8
0.5	250.25	1	250.25	1
0.6	300.20	12	250.25	8
0.7	350.15	22	250.25	14
0.8	400.10	43	250.25	25
0.9	450.05	103	250.25	57

Number of iterations of the basic scheme necessary for convergence depending on the choice of the reference material $\mathbb{C}^0$ and the volume fractions c_1 and $c_2 = 1 - c_1$

$$\frac{\left|\left\|F^{i+1}\right\| - \left\|F^{i}\right\|\right|^2}{\left\|F^1\right\|^2} < \varepsilon, \tag{25}$$

but no extra storage. Since $\left|\left\|F^{i+1}\right\| - \left\|F^{i}\right\|\right| \leq \left\|F^{i+1} - F^{i}\right\|$ the sequence (F^i) cannot converge if our criterion fails. Our criterion also applies to the two linear fixed point solvers presented in the succeeding sections.

3.2 Newton–Raphson method

To solve the nonlinear Lippmann–Schwinger Eq. (8) the Newton–Raphson method generates a sequence of deformation gradients F^i, related by $F^{i+1} = F^i + \Delta F^{i+1}$, where each ΔF^{i+1} solves the linear equation

$$\left(\mathbb{I} + \Gamma^0 : \left[\frac{dP}{dF}(F^i) - \mathbb{C}^0\right]\right) : \Delta F^{i+1} = \\ \bar{F}_n - \bar{F}^i - \Gamma^0 : P(F^i), \tag{26}$$

with $\mathbb{I}$ denoting the identity tensor on 2nd-order tensors, at the load step $\bar{F}_n$. The condition number of this linear system depends strongly on the current configuration F^i and can change significantly throughout the Newton–Raphson process. In the subsequent Sects. 3.2.1, 3.2.2, 3.2.3, and 3.2.4 we will discuss methods to solve this linear equation efficiently under the working assumption that $dP/dF(F^i)$ is positive definite. We will discuss the indefinite case thereafter, see Sect. 3.2.7.

For the convenience of the reader, we include the Newton–Raphson pseudocode for multiple load steps, see Algorithm 3, where we use the Moulinec–Suquet iterate with nonconstant right hand side to change between the load steps. Conditions for convergence of the Newton–Raphson method are addressed by the Newton–Kantorovich Theorem [35,36]. The Newton–Raphson method requires storing two deformation gradients, i.e. 18 scalars per voxel, plus possibly additional memory for the linear solver.

Algorithm 3 Newton–Raphson method (multiple load steps)

```
$F \leftarrow 0$
for $n \in \{0, \dots, n_{\max}\}$ do
    $F \leftarrow$ MSiterate($F$,$P$,$\mathbb{C}^0$,$\bar{F}_n$)  ▷ After this step we have $\bar{F} = \bar{F}_n$
    repeat
        $\Delta F \leftarrow -\left(\mathbb{I} + \Gamma^0 : \left[dP/dF(F) - \mathbb{C}^0\right]\right)^{-1} : \Gamma^0 : P(F)$
        $F \leftarrow F + \Delta F$
    until $\|\Delta F\| / \|\bar{F}_n\| < \delta$
end for
return $F$
```

3.2.1 Newton–Moulinec–Suquet method

The linear Eq. (26) can be solved analogously to the basic scheme described above using Algorithm 4 as proposed by Lahellec, Moulinec, and Suquet [25]. For a hyperelastic material the tensor field $dP/dF(F)$ satisfies the major symmetry. Suppose furthermore there are positive constants C, c, s.t.

Algorithm 4 Linear basic scheme [31]

```
$\Delta F \leftarrow 0$
repeat
    $\Delta F \leftarrow P(F) + (dP/dF(F) - \mathbb{C}^0) : \Delta F$
    $\Delta F \leftarrow$ FFT($\Delta F$)
    $\Delta F \leftarrow -\hat{\Gamma}^0 : \Delta F, \quad \Delta F(0) = 0$
    $\Delta F \leftarrow$ FFT$^{-1}$($\Delta F$)
until Convergence
return $\Delta F$
```

$$c\, G : G \leq G : dP/dF(F) : G \leq C\, G : G, \tag{27}$$

for all $G \in \mathbb{R}^{d\times d}$. Then the reference material $\mathbb{C}^0 = \frac{c+C}{2}\,\mathbb{I}$ leads to the estimate

$$\left\|\Delta F^{i+1,k} - \Delta F^{i+1}\right\|_{L^2} \leq \left(\frac{\kappa-1}{\kappa+1}\right)^k \left\|\Delta F^{i+1,0} - \Delta F^{i+1}\right\|_{L^2}, \tag{28}$$

where ΔF^{i+1} denotes the exact solution to Eq. (26) and $\kappa = C/c$.

Since the Moulinec–Suquet iteration operates in place, the Newton–Moulinec–Suquet method can be implemented storing two deformation gradients, i.e. 18 scalars per voxel, only.

3.2.2 Newton–Eyre–Milton method

To accelerate the basic scheme faster linear solver have been developed. Eyre–Milton [14] proposed to rewrite the equation

$$(\mathbb{I}+\Gamma^0 : [dP/dF(F)-\mathbb{C}^0]) : \Delta F = \bar{F}_n - \bar{F} - \Gamma^0 : P(F) \tag{29}$$

using the operator identity

$$\begin{aligned}(\mathbb{I} - YZ) : (dP/dF(F) + \mathbb{C}^0) = \\ 2\mathbb{C}^0 : (\mathbb{I} + \Gamma^0 : [dP/dF(F) - \mathbb{C}^0]),\end{aligned} \tag{30}$$

where

$$Y = \mathbb{I} - 2\mathbb{C}^0 : \Gamma^0, \tag{31}$$

$$Z = (dP/dF(F) - \mathbb{C}^0) : (dP/dF(F) + \mathbb{C}^0)^{-1}. \tag{32}$$

See also [26,28] for a relaxed version of the method. Thus, the following fixed point equation has to be solved

$$Q = Y : Z : Q + 2\mathbb{C}^0 : (\bar{F}_n - \bar{F}) - 2\mathbb{C}^0 : \Gamma^0 : P(F) \tag{33}$$

and ΔF is recovered via $\Delta F = (dP/dF(F) + \mathbb{C}^0)^{-1} : Q$. Under the assumption (27) the reference material $\mathbb{C}^0 = \sqrt{cC}\,\mathbb{I}$ guarantees the estimate

$$\|Q^{i+1,k} - Q^{i+1}\|_{L^2} \leq \left(\frac{\sqrt{\kappa}-1}{\sqrt{\kappa}+1}\right)^k \left\|Q^{i+1,0} - Q^{i+1}\right\|_{L^2} \tag{34}$$

with $\kappa = C/c$. Compared to the basic scheme, the Eyre–Milton scheme converges significantly faster [14,26,28].

A fast and memory-efficient method is obtained by rewriting (33) in the form

$$Q = Y : (ZQ + P(F)) + 2\mathbb{C}^0 : (\bar{F}_n - \bar{F}) - P(F). \tag{35}$$

This leads to the Algorithm 5.

Analogously to the Moulinec–Suquet iteration the Eyre–Milton scheme iterates in place, and no additional storage is necessary. Thus, the Newton–Eyre–Milton method requires storing two deformation gradients, i.e. 18 scalars per voxel.

Algorithm 5 Eyre–Milton linear solver for Newton–Raphson

```
NREMsolver($F$,$P$,$\mathbb{C}^0$)
$\Delta F \leftarrow 0$
repeat
    $\Delta F \leftarrow P(F) + (dP/dF(F) + \mathbb{C}^0) : \Delta F$
    $\Delta F \leftarrow$ FFT($\Delta F$)
    $\Delta F \leftarrow \Delta F - 2\mathbb{C}^0 : \hat{\Gamma}^0 : \Delta F$
    $\Delta F \leftarrow$ FFT$^{-1}$($\Delta F$)
    $\Delta F \leftarrow \Delta F - P(F)$                ▷ $\bar{F} = \bar{F}_n$ in Algorithm 3
    $\Delta F \leftarrow (dP/dF(F) + \mathbb{C}^0)^{-1} : \Delta F$
until Convergence.
return $\Delta F$
```

Vinogradov and Milton [44] introduced a variant of this method for nonlinear thermoelasticity at small deformations. Instead of computing the increment ΔF^{i+1}, they solve for $F^{i+1} = F^i + \Delta F^{i+1}$ directly using the Eyre–Milton method.

3.2.3 Newton–Krylov method

Zeman, Vondřejc, Novák, and Marek [48] as well as Brisard and Dormieux [8,9] advocate utilizing Krylov subspace methods for the solution of linear systems of the type (26). The conjugate gradient method of Hestenes and Stiefel [18] has been demonstrated to be a powerful method for solving linear Lippmann–Schwinger equations, and is virtually independent of the reference material $\mathbb{C}^0$ [45]. The idea of combining the Newton–Raphson method with Krylov subspace solvers has been initiated for nonlinear problems at small deformation by Gélébart and Mondon–Cancel [17]. The iterates generated by the conjugate gradient method satisfy the error estimate

$$\begin{aligned}&\left\|\Delta F^{i+1,k} - \Delta F^{i+1}\right\|_* \leq \\ &2\left(\frac{\sqrt{\text{cond}}-1}{\sqrt{\text{cond}}+1}\right)^k \left\|\Delta F^{i+1,0} - \Delta F^{i+1}\right\|_*,\end{aligned} \tag{36}$$

where the $*$-subscript indicates the dP/dF-weighted L^2-norm and

$$\begin{aligned}\text{cond} = \inf\Bigg\{\frac{C}{c} \,\Bigg|\, &c\,\|\nabla u\|_{L^2} \leq \|\nabla u\|_{L^2(dP/dF(F))} \\ &\leq C\,\|\nabla u\|_{L^2}, \quad \forall u \in \left[H^1_\#(\mathbb{T}^d)\right]^d\Bigg\},\end{aligned} \tag{37}$$

provided cond is finite.

Although the error estimates (34) for Eyre–Miton and (36) for CG look similar, κ and cond differ in general. Indeed, cond $\leq \kappa$ by construction, but cond can be significantly smaller. Furthermore, in every iteration CG eliminates the largest eigenvalue, so that the estimate (36) improves with every step, see [3].

However, there is a downside because the CG method needs the storage of four[3] deformation gradients, raising the required storage of the Newton–Krylov method to five deformation gradients (or 45 scalars per voxel). The CG method for the linearized Lippmann–Schwinger Eq. (26) is recalled in Algorithm 6, cf. [6].

3.2.4 Memory-efficient Newton–Krylov method

Exploiting the special structure of the Green's operator (9) the need for additional storage can be drastically reduced.

---

[3] It is possible to work with three deformation gradients but only at the expense of two matrix operations per iteration.

Algorithm 6 CG method for Newton–Raphson

```
NRCGsolver($F$,$P$,$\mathbb{C}^0$)
$X \leftarrow -P(F)$                                   ▷ $\bar{F} = \bar{F}_n$ in Algorithm 3
$X \leftarrow \mathrm{FFT}(X)$
$X \leftarrow \hat{\Gamma}^0 : X$
$X \leftarrow \mathrm{FFT}^{-1}(X)$
ApplyOperator($X$, $R$)
$Q \leftarrow R$
$\gamma \leftarrow \|R\|^2_{L^2}$
repeat
    ApplyOperator($Q$, $W$)
    $\alpha \leftarrow \langle Q, Q - W\rangle_{L^2}$
    $\alpha \leftarrow \gamma/\alpha$
    $X \leftarrow X + \alpha Q$
    $R \leftarrow R - \alpha Q + \alpha W$
    $\delta \leftarrow \|R\|^2_{L^2}$
    $\beta \leftarrow \delta/\gamma$
    $\gamma \leftarrow \delta$
    $Q \leftarrow R + \beta Q$
until Convergence
return $X$
ApplyOperator(Q,W)
$W \leftarrow -(dP/dF(F) - \mathbb{C}^0) : Q$
$W \leftarrow \mathrm{FFT}(W)$
$W \leftarrow \hat{\Gamma}^0 : Q$
$W \leftarrow \mathrm{FFT}^{-1}(W)$
```

Indeed, each of the four deformation gradients arise as gradients of displacements, i.e.

$$X = \nabla x, \quad R = \nabla r, \quad Q = \nabla q, \quad W = \nabla w \tag{38}$$

and $\Gamma^0 = \nabla G^0 \mathrm{Div}$. Furthermore, we need to compute the inner product

$$\langle \nabla d, \nabla y \rangle = \int_{\mathbb{T}^d} \nabla d : \nabla y \, dX \tag{39}$$

cheaply for vector fields d and y. If d and y are written[4] as

$$d(X) = \sum_{\xi \in 2\pi\mathbb{Z}^d/L} \hat{d}(\xi) \exp(iX \cdot \xi), \tag{40}$$

$$y(X) = \sum_{\xi \in 2\pi\mathbb{Z}^d/L} \hat{y}(\xi) \exp(iX \cdot \xi) \tag{41}$$

for $X \in \mathbb{T}^d = \mathbb{R}/L_1\mathbb{Z} \times \cdots \times \mathbb{R}/L_d\mathbb{Z}$ and the short notation

$$2\pi\mathbb{Z}^d/L = \left\{ \left(\frac{2\pi z_1}{L_1}, \ldots, \frac{2\pi z_d}{L_d} \right) \;\middle|\; (z_1, \ldots, z_d) \in \mathbb{Z}^d \right\} \tag{42}$$

Parseval's theorem enables us to write

$$\langle \nabla d, \nabla y \rangle = |\mathbb{T}^d| \sum_{\xi \in 2\pi\mathbb{Z}^d/L} \|\xi\|^2 \hat{d}(\xi) \cdot \overline{\hat{y}(\xi)}, \tag{43}$$

where $z \mapsto \bar{z}$ denotes complex conjugation. In particular to save required FFTs, it seems convenient to work in Fourier space throughout. Then, the evaluation of inner products like $\langle \nabla d, \nabla y \rangle$ reduces to a simple sum that can be computed in place. Expressions of the Fourier coefficients of the operators ∇, G^0 and Div can be found in Appendix 7. The Algorithm 7 generates iterates related by (38) to the iterates of Algorithm 6. In particular, the convergence speed is preserved.

Algorithm 7 memory-efficient CG for Newton-Raphson

```
NRCGsolver2[$F$,$P$,$\mathbb{C}^0$]
$W \leftarrow -P(F)$                                   ▷ $\bar{F} = \bar{F}_n$ in Algorithm 3
$W \leftarrow \mathrm{FFT}(W)$
$x \leftarrow \widehat{G^0}\widehat{\mathrm{Div}}\, W$
ApplyReducedOperator($x$, $W$, $r$)
$q \leftarrow r$
$\gamma \leftarrow$ Innerproduct($r$, $r$)
repeat
    ApplyReducedOperator($q$, $W$, $w$)   ▷ $w$ uses the memory of the
      first three components of $W$
    $\alpha \leftarrow$ Innerproduct($q$, $q - w$)
    $\alpha \leftarrow \gamma/\alpha$
    $x \leftarrow x + \alpha q$
    $r \leftarrow r - \alpha q + \alpha w$
    $\delta \leftarrow$ Innerproduct($r$, $r$)
    $\beta \leftarrow \delta/\gamma$
    $\gamma \leftarrow \delta$
    $q \leftarrow r + \beta q$
until Convergence.
$W \leftarrow \widehat{\nabla} x$
return $\mathrm{FFT}^{-1}(W)$
ApplyReducedOperator(q,W,w)
$W \leftarrow \widehat{\nabla} q$
$W \leftarrow \mathrm{FFT}^{-1}(W)$
$W \leftarrow -(dP/dF(F) - \mathbb{C}^0) : W$
$W \leftarrow \mathrm{FFT}(W)$
$w \leftarrow \widehat{G^0}\widehat{\mathrm{Div}}\, W$
Innerproduct(q,r)
return $\sum_\xi \|\xi\|^2 q : \bar{r}$          ▷ $z \mapsto \bar{z}$ denotes complex conjugation
```

It is important to note that memory for the displacements x, q, r and the deformation gradient W needs to be allocated. In particular, the displacement w occupies a third of the memory of W. This needs to be kept in mind writing the function ApplyReducedOperator(q, W, w).

In contrast to the naive CG implementation, our memory-efficient version of the Newton–Krylov method requires storing two deformation gradients and three displacements, i.e. 27 doubles per voxel, and amounts to a 40 % memory reduction.

---

[4] One should not confuse the position variable X with the solution vector X from (38).

3.2.5 Intrinsic instability of linear fixed point solvers

In this section we will discuss an instability phenomenon related to the choice of reference material for the linear fixed point solvers used in Sects. 3.2.1 and 3.2.2. These problems are not present for the Krylov methods.

If the reference configuration has no residual stresses at the undeformed state $F = I$, with I denoting the 2nd-order identity tensor, $dP/dF(I)$ defines pointwise a linear elastic material. In particular, dP/dF satisfies minor and major symmetries. As a consequence $dP/dF(I)$ is degenerate in the sense that it does not satisfy the inequality (3).

In linear elasticity instead of (3) one works with the weaker inequality

$$c\varepsilon : \varepsilon \leq \varepsilon : \mathbb{C} : \varepsilon \leq C\varepsilon : \varepsilon, \quad \varepsilon \in \mathbb{R}^{d\times d}, \varepsilon^T = \varepsilon, \qquad (44)$$

for positive constants C and c independent of ε and a linearly elastic reference material like $2\mu\mathbb{I}^S$, where $\mathbb{I}^S$ is the identity on symmetric matrices. If F is slightly perturbed from the identity, $dP/dF(F)$ loses its minor symmetry, and usually becomes non-degenerate in the sense of (3). Then, linearly elastic reference materials do not lead to the bounds (28) and (34), which are only valid for reference materials that are non-degenerate on the whole of $\mathbb{R}^{d\times d}$.

On the other hand, choosing the reference material of the type $2\mu\mathbb{I}$ with $\mathbb{I}$ being the identity tensor on 2nd-order tensors leads to the bounds (28) and (34), but these bounds becomes arbitrarily bad as $F \to I$. More precisely, let (F_k) be a sequence of sufficiently smooth deformations converging to I in C^1. Then, $\kappa(F_k) \to \infty$ as $k \to \infty$. Similar phenomena can occur in the vicinity of other states exhibiting low stresses or particular symmetries.

The phenomenon just described is intrinsic and cannot be easily repaired. Furthermore, the phenomenon is not present in linear elasticity. In particular, the Eyre–Milton scheme exhibits instabilities and loses a lot of its computational power compared to the linear case. We will see this in the computational section.

It is important to note that for the sequence (F_k) above the Kroylov methods has no problems. Indeed, cond(I) is finite, and cond$(F_k) \to$ cond(I) as $k \to \infty$.

3.2.6 Comparison

With our convergence criterion the basic scheme for the nonlinear Lippmann–Schwinger equation only needs storage for the solution, i.e. one (asymmetric) deformation gradient. Application of the Newton–Raphson methods combined with linear fixed point solvers requires one additional deformation gradient for the solution increment. The CG method for solving the linearized Lippmann–Schwinger equation demands three additional deformation gradients, whereas our adapted Newton–Krylov method gets by with three additional displacements. In Table 2 we summarize the memory usage at Double-precision (8 bytes = 64 bits) and the number of iterations necessary for convergence. For the FFT-based methods we use the following abbreviations

Table 2 Computational costs of the different FFT-based methods

FFT-based method	Memory usage per voxel [byte]	Number of iterations [$-$]
MS	72	$\sim \kappa$
NR	144	$\sim \kappa$
NE	144	$\sim \sqrt{\kappa}$
NK	360	$\sim \sqrt{\text{cond}}$
NK2	216	$\sim \sqrt{\text{cond}}$

κ denotes the contrast, i.e. the quotient of the largest and smallest eigenvalue of dP/dF in $\mathbb{T}^d$. cond is the condition number of the resulting linear system

MS	Moulinec–Suquet for the nonlinear Lippmann–Schwinger equation
NR	Moulinec–Suquet for the linearized Lippmann–Schwinger equation
NE	Eyre–Milton for the linearized Lippmann–Schwinger equation
NK	CG for the linearized Lippmann–Schwinger equation
NK2	memory-efficient CG for the linearized Lippmann–Schwinger equation

3.2.7 Indefinite $dP/dF(F)$

The linear solvers for the Newton–Raphson procedure presented so far assume positive definite linearized first Piola–Kirchhoff stress tensor dP/dF during the Newton–Raphson steps. This assumption is often encountered in practice, and can be easily checked. Indeed, to determine the reference material it is necessary to compute the eigenvalues of $dP/dF(F^i)$ for every voxel. If these eigenvalues are all positive, the linear solvers can be used without second thought.

If negative eigenvalues appear, the resulting linear systems are not necessarily positive definite, and convergence cannot be guaranteed in general. Such systems arise frequently in the presence of (continuous or discrete) symmetries or buckling. In Sect. 5 we will encounter such indefinite systems. In our experience there are three remedies to this difficulty.

1. Use the basic scheme until the linear system becomes positive again.
2. Use the linear solvers, and disregard the negative eigenvalues in the computation of the reference material.

3. m Use a Krylov subspace solver that can handle indefinite systems, like SYMMLQ or MINRES [37].

Our numerical experiments in Sect. 5 indicate that 2. suffices to handle the problems in this article.

4 St.Venant–Kirchhoff laminate

We consider a laminate consisting of two elastic materials with volume fractions c_1 and c_2, respectively. The ratio of the volume fractions corresponds to the ratio of the layer thicknesses, i.e. $c_1/c_2 = d_1/d_2$ (see Fig. 1).

The elastic behavior of the layers is assumed to be of the St.Venant–Kirchhoff type

$$S = \mathbb{C} : E, \tag{45}$$

which means that the 2nd-Piola–Kirchhoff stress tensor $S = \det(F)F^{-1}\sigma F^{-T}$ is a linear function of the Green' strain tensor $E = (F^T F - I)/2$. Assuming a hyperelastic material behavior implies that the stiffness tensor $\mathbb{C}$ has the major symmetry. In the isotropic case, the stiffness tensor is given by $\mathbb{C} = \lambda I \otimes I + 2\mu\mathbb{I}^S$ with $\mathbb{I}^S$ being the identity tensor on 2nd-order symmetric tensors. The two Lamé moduli λ and μ specify completely the physically linear elastic behavior. They are related to Young's modulus and Poisson's ratio by $\lambda = \nu E/(1+\nu)/(1-2\nu)$ and $\mu = E/(1+\nu)/2$, respectively.

The St.Venant–Kirchhoff type constitutive equation has been noted to exhibit general deficiencies. Reasons are the lack of rank-one convexity [4,7,12,22] which implies non-polyconvexity and the physically incorrect behavior of the stored energy function $\bar{W}(F) = \lambda/2(\operatorname{tr} E)^2 + \mu \operatorname{tr}(E^2)$ for $\det F \to 0^+$, i.e. $\lim_{\det F \to 0^+} \bar{W}(F) \neq +\infty$ [12]. Therefore, the existence of minimizers of the underlying boundary value problem is not guaranteed at large strains. Nevertheless, the St. Venant–Kirchhoff model gives reasonable results in the small strain—large displacement regime and allows for the derivation of analytical solutions in Sect. 4.1, and can thus serve as a benchmark for the analysis of geometrically non-linear FFT-based schemes. In contrast to the derivation of the analytical solutions these schemes do not depend on the linear stress–strain relation of the St. Venant–Kirchhoff model and for example have been successfully applied to compressible Mooney–Rivlin materials [25].

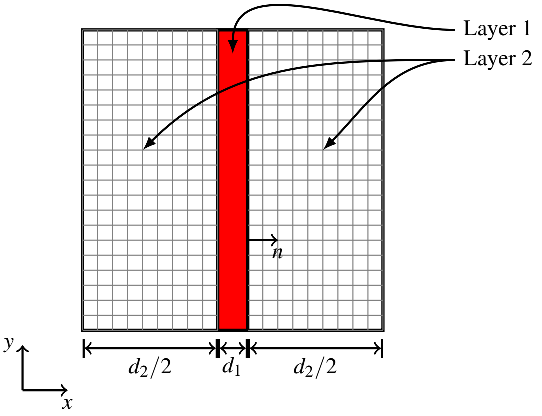

Fig. 1 Laminate

The effective deformation gradient $\bar{F}$ of the laminate is given by its volume average in the reference configuration. Hence, it is given by $\bar{F} = c_1 F^1 + c_2 F^2$, where F^1 and F^2 denote the phase averages of the deformation gradient in phase 1 and 2.

4.1 Analytical solution

In the following, it will be assumed that for given $\bar{F}$ the two layers of the laminate deform homogeneously. In this case the equilibrium conditions are satisfied trivially inside the layers. The static equilibrium condition for a singular interface—here the interface between the two layers—translates into the requirement that the traction vector is continuous [40,43]. In a Lagrangian setting this condition reads

$$P^1 n = P^2 n. \tag{46}$$

The vector n is the unit-normal vector of the interface (see Fig. 1). On singular interfaces, the kinematic compatibility condition implies that the jump of the deformation gradient is a tensor of rank one and is of the following form

$$F^2 = F^1 + a \otimes n \tag{47}$$

[40,43]. Combining the equilibrium condition, the kinematic compatibility condition, the constitutive equations and the boundary conditions result in the following 21 equations

$$F^1(\mathbb{C}_1 : ((F^1)^T F^1 - I))n = F^2(\mathbb{C}_2 : ((F^2)^T F^2 - I))n, \tag{48}$$

$$\bar{F} = c_1 F^1 + c_2 F^2, \tag{49}$$

$$F^2 = F^1 + a \otimes n \tag{50}$$

for the 21 unknowns F^1, F^2 and a. The solution of the equations can be simplified by eliminating F^1 and F^2 and obtaining three cubic equations in the components of the vector a. The solution for a can be used to determine explicitly the deformation gradients in the layers as a function of a

$$F^1 = \bar{F} - c_2 a \otimes n, \qquad F^2 = \bar{F} + c_1 a \otimes n. \tag{51}$$

In Fig. 2 the solutions for the deformation gradients in the layers are shown for different deformation processes in terms of $\bar{F}$. The cubic equation for a is solved numerically, then the deformation gradients in the layers are determined. The elastic constants in the layers are chosen as follows: $\lambda_1 = 50\,\text{GPa}$,

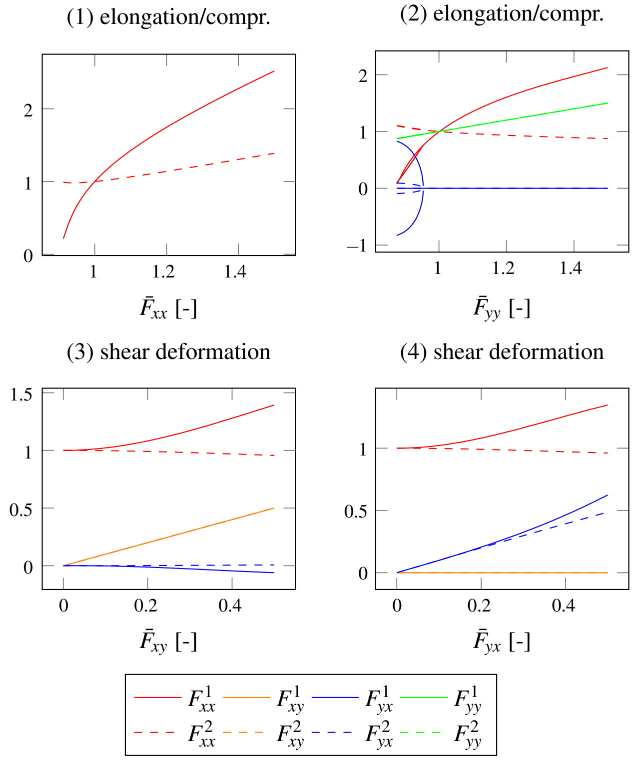

Fig. 2 Microscopic deformation gradient components of the analytical solutions subject to prescribed macroscopic deformation gradients

$\mu_1 = 25$ GPa, $\lambda_2 = 1000$ GPa, $\mu_2 = 25$ GPa. The volume fractions are given by $c_1 = 1/10$ and $c_2 = 9/10$, respectively. In the subsequent discussion only solutions with positive eigenvalues of the deformation gradient are considered.

1. The effective deformation gradient corresponds to a uniaxial elongation or compression in the normal direction of the layers: $\bar{F} = I + \varepsilon e_x \otimes e_x$. The parameter ε represents the Biot strain. It can be seen that the two layers are subjected to the same deformation mode as the composite. The only difference is the intensity of elongation in e_x direction which is larger in the soft layer 1. The solution is unique in the considered range of ε.
2. The effective deformation gradient corresponds to a uniaxial elongation or compression in the tangential direction of the layers: $\bar{F} = I + \varepsilon e_y \otimes e_y$. Obviously the two layers are not subjected to the same deformation mode as the composite. In the elongation direction the stretches are identical. In the cross direction, layer 1 shows an elongation whereas layer 2 shows a contraction. No shear deformation is induced for macroscopic elongation. Under compression, the solution is unique up to a compression of approximately $\varepsilon = -0.046639$, then three solutions exist, i.e. we encounter a bifurcation in the sense of a radical change of the characteristics of the energy landscape. These three solutions $a = (a_x, a_y, 0)$ correspond to the critical points of the total hyperelastic energy density

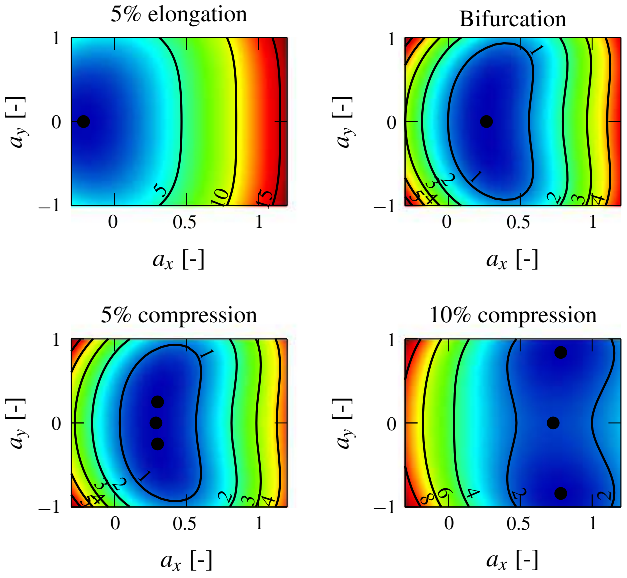

Fig. 3 Critical points of the elastic energy density $f(F)/|\mathbb{T}^d|$ [GPa]

$$
\begin{aligned}
\frac{f(F)}{|\mathbb{T}^d|} &= \frac{1}{|\mathbb{T}^d|} \int_{\mathbb{T}^d} \bar{W}(F)\, dX \\
&= (1/16000)(-50760 a_x^3 + 13311 a_x^4 \\
&\quad +13311 a_y^4 + 1910000 \varepsilon^2 (2+\varepsilon)^2 \\
&\quad -360 a_x (141 a_y^2 - 1900 x (2+\varepsilon)) \\
&\quad +1800 a_y^2 (10 + 39 \varepsilon (2+\varepsilon)) + 18 a_x^2 \\
&\quad (1479 a_y^2 + 100(78 + 29 \varepsilon (2+\varepsilon)))), \qquad (52)
\end{aligned}
$$

which is invariant with respect to $a_y \mapsto -a_y$. Energy landscapes for varying compression are displayed in Fig. 3. The solution which exists for the complete range of compression shows equal stretches in the compression direction and a compression in layer 1 and a elongation in layer 2 in the cross direction. The symmetric second and third solutions occurring for larger amounts of compression exhibit a reduced cross directional stretch in both layers and a significant shear mode in both layers. Both shears have the composite normal $e_x = n$ as shear plane normal and the composite tangential direction e_y as shear direction. Since the energy density is smaller for the two solutions with shear modes (Fig. 4) these are the physically correct solution under compression.
3. The effective deformation gradient corresponds to a simple shear deformation: $\bar{F} = I + K e_x \otimes e_y$. The shear plane normal is e_y. The shear direction is given by e_x. The amount of shear is specified by the shear number K. The macroscopic shear deformation induces in both

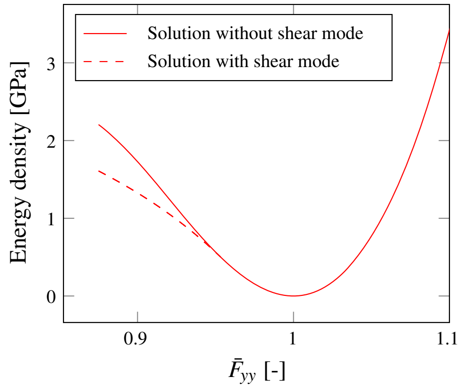

Fig. 4 Elastic energy density $f(F)/|\mathbb{T}^d|$ [GPa] of the analytical solutions under uniaxial elongation/compression in the tangential direction of the layers

layers stretches in the composite normal direction. The shear deformation F_{xy} is identical in both layers. The shear deformations F_{yx} are slightly different in the layers.

4. The effective deformation gradient corresponds also to a simple shear deformation: $\bar{F} = I + K e_y \otimes e_x$. The shear plane normal is e_x. The shear direction is given by e_y. The macroscopic shear deformation induces stretches in the composite normal direction in both layers. The shear deformation F_{yx} is identical in both layers for small and intermediate shear numbers K. For large K the components F_{yx} differ in both layers. In contrast to case 3, no shear deformations F_{xy} are induced.

The bifurcation behavior of the laminate is similar to that of a rigid rod attached to a wall with a torsional spring. For a compression loading there is a first loading range with only one solution, which is furthermore stable. After passing a critical load there are two symmetric stable solutions (deflected) and an unstable one (non-deflected). The two deflected solutions are physically equivalent due to the symmetry of the laminate problem reflected both in the microstructure and in the boundary condition, compare Fig. 2.

4.2 Effective behavior

The effective stiffness of a laminate of two isotropic linearly elastic phases satisfying $\mu_1 = \mu_2$ is also isotropic. One might wonder whether this result extends to large deformations, replacing isotropic linearly elastic materials by isotropic St. Venant–Kirchhoff materials.

In the linear elastic case one obtains, following [27], $\mu^{\mathrm{eff}} = 25$GPa and $\lambda^{\mathrm{eff}} = 6350/13$GPa. Since for small deformations $F \to I$ the second Piola–Kirchhoff stress $S = \mathbb{C} : E$ converges to the linear elastic material law, an effective St. Venant–Kirchhoff material (45) would have to be defined by the effective linear elastic material parameters, i.e. $\mathbb{C}^{\mathrm{eff}} = \lambda^{\mathrm{eff}} I \otimes I + 2\mu^{\mathrm{eff}} \mathbb{I}^S$.

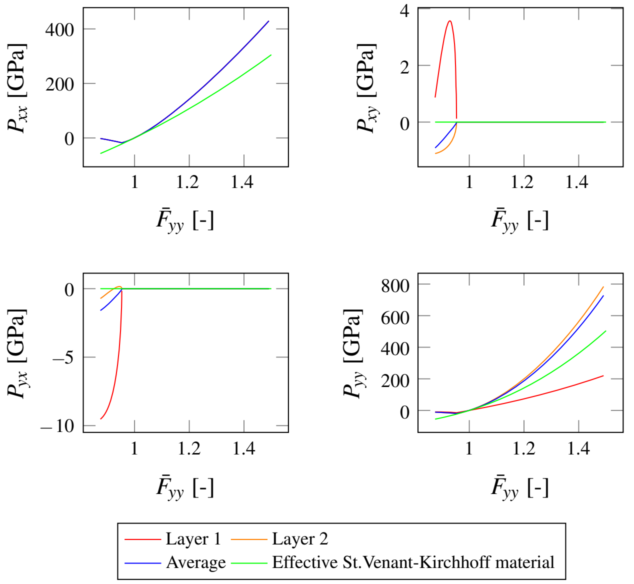

Fig. 5 First Piola–Kirchhoff stress for elongation/compression in the tangential direction of the layers

Clearly, a homogeneous isotropic St. Venant–Kirchhoff material would behave in the same way for elongation resp. compression in all space directions. Since the laminate shows bifurcations of the solution only under compression in the tangential direction of the layers (Fig. 2, (1), (2)) the effective St.Venant–Kirchhoff material can not approximate the laminate for large strains.

Nevertheless, Fig. 5 shows that the average of the first Piola–Kirchhoff stress $\bar{P}$ of the laminate and the effective first Piola–Kirchhoff stress $P^{\mathrm{eff}} = \bar{F}\mathbb{C}^{\mathrm{eff}} : (\bar{F}^T\bar{F} - I)/2$ are in good agreement up to an elongation of approximately 10 % and up to a compression of approximately 5 %.

5 Numerical studies

In this section we will first numerically deform the St. Venant–Kirchhoff laminate discussed in Sect. 4. If the layers are aligned with the coordinate axis the geometry can be exactly resolved by a voxel discretization and we do not have to deal with voxel resolution effects. Aterwards, we will apply the FFT-based methods to a complex microstructure typical for glass fiber reinforced plastics. The numerical examples in this section were implemented and tested with the commercial code FeelMath, distributed as part of GeoDict.

Due to robustness issues we used for NE the same reference material as for NR , i.e. $\mathbb{C}^0 = \frac{c+C}{2}$ Id, cf. Sect. 3.2.2 and the instability discussion in Sect. 3.2.5.

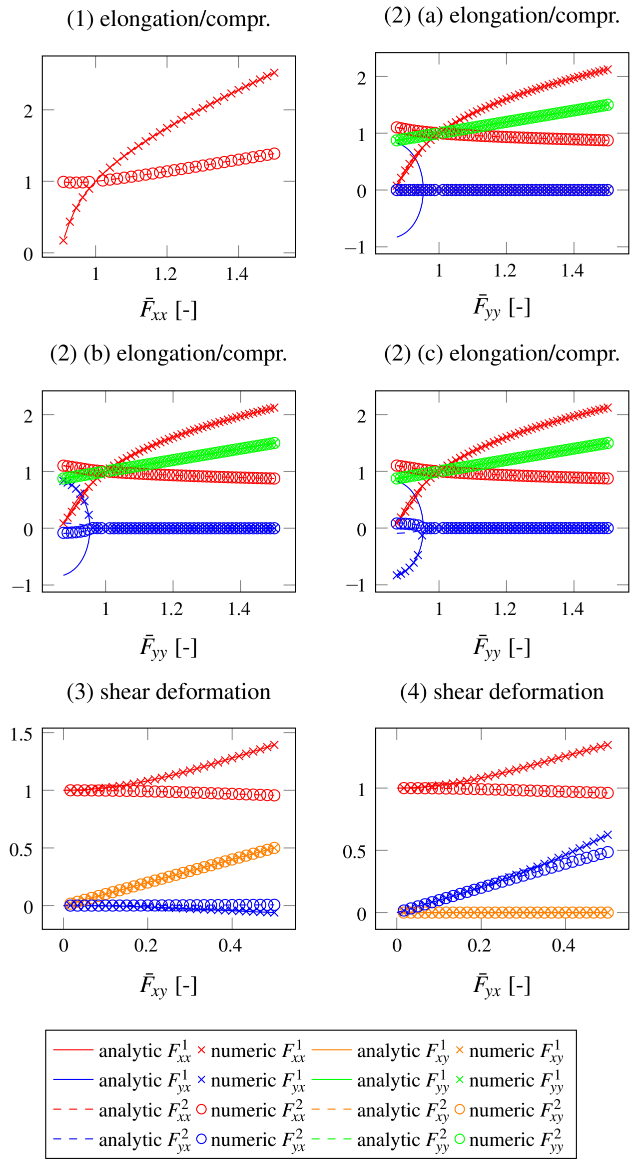

Fig. 6 Comparison of numerical and analytical solutions. Microscopic deformation gradient components subject to prescribed macroscopic deformation gradients

5.1 St. Venant–Kirchhoff laminate

The numerical solution of the Lippmann–Schwinger Eq. (8) confirms that the two layers of the laminate deform homogeneously. In Fig. 6 the solutions for the deformation gradients in the layers are compared with the corresponding solutions of the Lippmann–Schwinger equation for different deformation processes in terms of $\bar{F}$. For all deformations the solution of the different FFT-based methods coincide. Therefore only one numerical result will be compared to the solution of the analytical Eqs. (48), (49), (50) in Fig. 6.

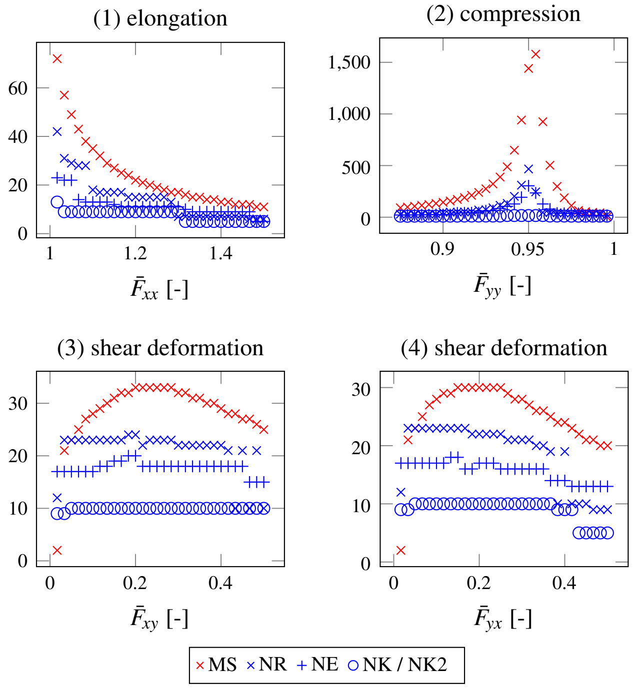

Fig. 7 Applications of the basic scheme

1. The numerical solution coincides with the unique analytical solution for uniaxial elongation/compression in the normal direction of the layers: $\bar{F} = I + \varepsilon e_x \otimes e_x$.
2. There exist three different analytical solutions. The analytical solution without shear mode exists in the whole range of uniaxial elongation/compression in the tangential direction of the layers: $\bar{F} = I + \varepsilon e_y \otimes e_y$. Without perturbations the numerical solution coincides with this analytical solution (Fig. 6, (2) (a)). Since the energy density is smaller for the two analytical solutions with shear modes (Fig. 4) this is not the physically correct solution under compression. By small perturbations of the prescribed average deformation gradient $\bar{F} = I + \varepsilon e_y \otimes e_y \pm 0.01 e_y \otimes e_x$ both physical correct solutions can be obtained numerically (Fig. 6, (2) (b), (c)).
3. The numerical solution coincides with the unique analytical solution for a simple shear deformation: $\bar{F} = I + K e_x \otimes e_y$.
4. The numerical solution coincides with the unique analytical solution for a simple shear deformation: $\bar{F} = I + K e_y \otimes e_x$.

For all FFT-based methods used to solve the Lippmann–Schwinger Eq. (8) the CPU-Time is dominated by the number of applications of FFTs, which we measure in equivalent applications of the basic scheme ($\equiv$ 18 FFTs). Remarkably, this number does not depend on the grid spacing [31]. The number of applications of the basic scheme necessary for convergence ($\varepsilon = 10^{-5}$, $\delta = 10^{-2}$) is shown in Fig. 7 for

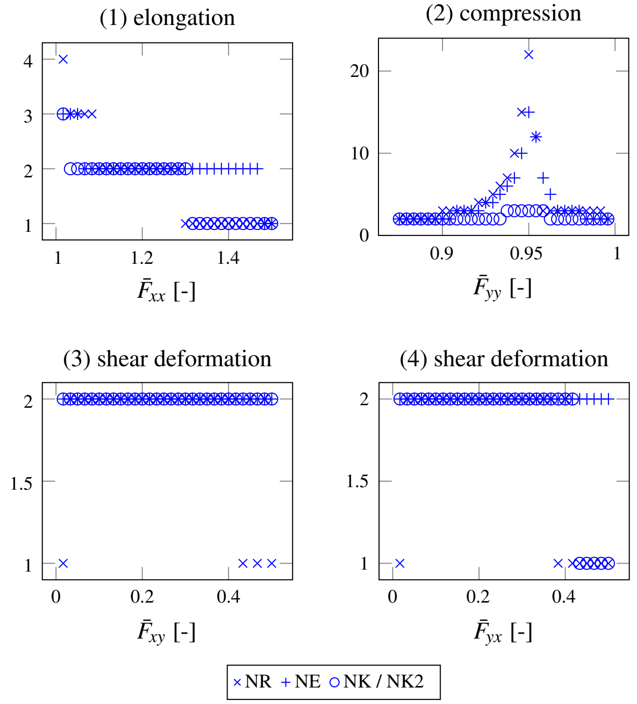

Fig. 8 Number of Newton–Raphson iterations

different deformation processes in terms of $\bar{F}$. The corresponding number of Newton–Raphson iterations is shown in Fig. 8.

1. MS needs approximately twice the number of applications of the basic scheme to compute uniaxial elongation in the normal direction of the layers: $\bar{F} = I + \varepsilon e_x \otimes e_x$. The number of Newton–Raphson iterations is higher for NR at the beginning of the deformation.
2. The number of applications of the basic scheme grows dramatically for uniaxial compression in the tangential direction of the layers with perturbation ($\bar{F} = I + \varepsilon e_y \otimes e_y \pm 0.01 e_y \otimes e_x$) when the shear mode starts to evolve. In Table 3 the iteration numbers at the onset of the bifurcation (Fig. 6, (2) (b)) are shown. Only the Newton–Krylov methods NK and NK2 need acceptable number of iterations for convergence.
3. The number of applications of the basic scheme of MS for a simple shear deformation $\bar{F} = I + K e_x \otimes e_y$ has its maximum when the she shear deformation F_{xy} evolves. For NR and NE and NK and NK2 the computational costs stay almost constant over the whole range of considered shearing.
4. The number of applications of the basic scheme of MS for a simple shear deformation $\bar{F} = I + K e_y \otimes e_x$ becomes maximal when the she shear deformation F_{xy} evolves. For NR and NE and NK and NK2 the computational costs stay almost constant over the whole range of considered shearing.

Table 3 Computational costs at the onset of the bifurcation during compression in the tangential direction of the layers

FFT-based method	Applications of the basic scheme [−]	Newton–Raphson iterations [−]
MS	1441	–
NR	467	22
NE	304	15
NK / NK2	16	3

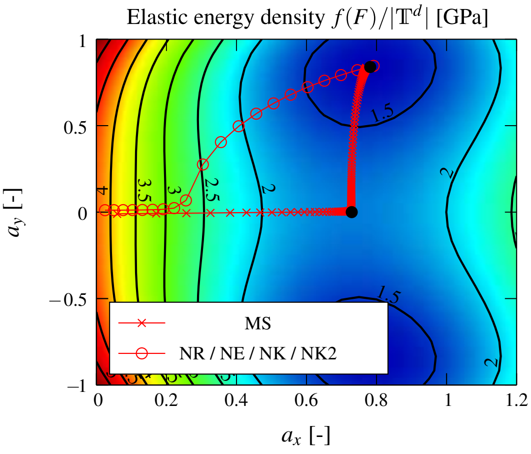

Fig. 9 Iterates of the FFT-based schemes for 10 % compression in tangential direction of the layers

The advantage of the Newton–Raphson iteration can also be seen for this simple example. In Fig. 9 we show both the iterates of MS and the Newton–Raphson method on a contour plot for the energy densitiy $f(F)/|\mathbb{T}^d|$ of the deformation (51) for 10 % compression in the tangential direction of the layers ($\bar{F} = I - 0.1 e_y \otimes e_y$). All iterates are represented by $a = (a_x, a_y, 0)$ satisfying (51). The iterates of MS have been obtained by using one load step, whereas the iterates of the Newton–Raphson methods are the projections of the solutions for multiple load steps.

5.2 Glas fiber reinforced plastic (GFRP)

The industrial-sized example of a glass fiber reinforced plastic (GFRP) shown in Figs. 10 and 11 was generated with GeoDict[5] by use of the algorithm described in [38]. The fiber volume fraction of the GFRP is 13 % and the fiber orientation tensor (see [1] for a definition) is given by

---

[5] www.geodict.com

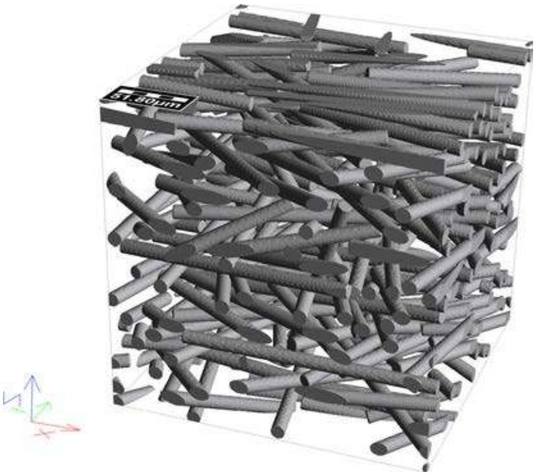

Fig. 10 GFRP microstructure

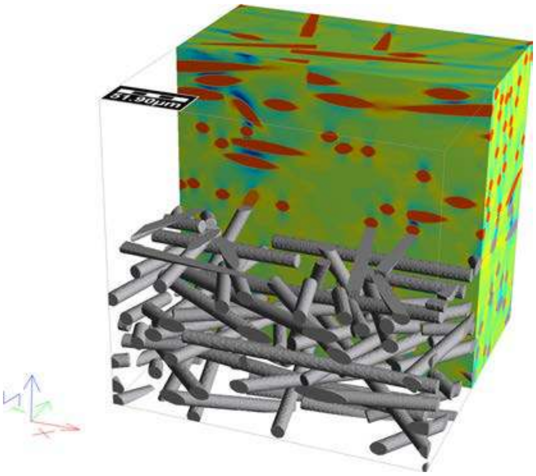

Fig. 11 Green Lagrange strain E_{zz} of the GFRP microstructure under compression $\bar{F}_{zz} = 0.95$

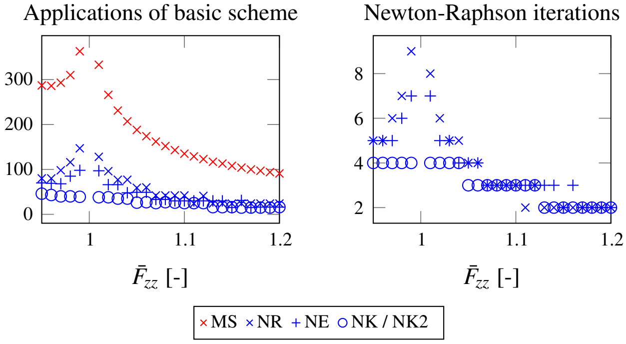

Fig. 12 Comparison of the computational costs for the realistic microstructure during elongation and compression in z-direction

Table 4 Computational costs for the first load increment $\bar{F}_{zz} = 0.99$

FFT-based method	Memory usage [GB]	Applicat. of the basic scheme $[-]$	Newton–Raphson iterations $[-]$
MS	9	363	–
NR	18	147	9
NE	18	98	7
NK	45	39	4
NK2	27	39	4

The fiber geometry (Fig. 10) was disretized with 512 × 512 × 512 voxels and the simulation was performed at Double-precision (8 byte = 64 bits)

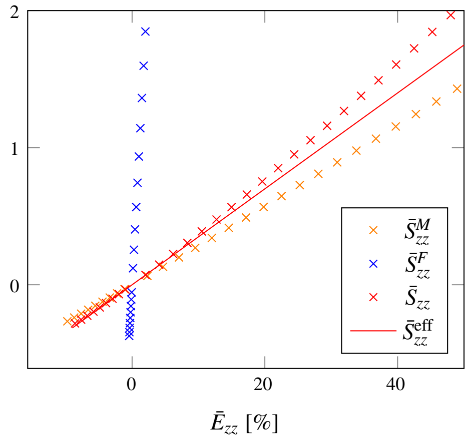

Fig. 13 Comparison of the GFRP with an effective St. Venant–Kirchhoff material. The superscripts M and F denote local averages over the matrix and fibers, respectively

$$\begin{pmatrix} 0.61 & 0 & 0 \\ 0 & 0.36 & 0 \\ 0 & 0 & 0.03 \end{pmatrix}. \tag{53}$$

This corresponds to a planar orientation state in the $x-y-$plane, where on average almost twice as many fibers point in the $x-$direction as in the $y-$direction. The elastic constants of the glass fibers and the plastic were chosen as follows: $E_F = 73$GPa, $\nu_F = 0.2$, $E_M = 1.665$GPa, $\nu_M = 0.36$. The applied effective deformation gradient $\bar{F}$ corresponds to a uniaxial elongation/compression in the normal direction of most of the fibers: $\bar{F} = I + \varepsilon e_z \otimes e_z$. We notice the following.

1. The results of the four different FFT-based methods for solving the nonlinear Lippmann–Schwinger equation for finite strain coincide.
2. Compression is more expensive than elongation (see Fig. 12).
3. The Newton–Krylov methods NK and NK2 need less computational effort than MS and NR and NE (see Fig. 12 and Table 4).
4. The behavior of the composite can only be approximated up to a deformation of about 10 % by an effective St.Venant–Kirchhoff material: Fig. 13 compares the average second Piola–Kirchhoff stress of the GFRP with the second Piola–Kirchhoff stress of the homogenous St. Venant–Kirchoff material $S^{\text{eff}} = \mathbb{C}^{\text{eff}} : E$. The effective

linear elastic stiffness $\mathbb{C}^{\mathrm{eff}}$ of the GFRP has been calculated numerically by the original FFT-based method of Moulinec and Suquet [30]. Following [19] the average Green-Langrange strain and the average second Piola–Kirchhoff stress are defined by $\bar{E} := (\bar{F}^T\bar{F} - I)/2$ and $\bar{S} := \bar{F}^{-1}\bar{P}$.

These observations agree with the lessons learned from deforming the laminate in the previous section.

6 Conclusion

In this article we carried over the FFT-based methods of Vinogradov and Milton [44] as well as of Gélébart and Mondon–Cancel [17] to the geometrically nonlinear case (Sects. 3.2.2 and 3.2.3). It turned out that the first looses its computational power compared to the case of small deformations (Sect. 3.2.5) and the second needs excessive memory (Table 2). Therefore, we have modified the latter (Sect. 3.2.4) and reduced the additional memory requirement of the CG method in the Newton–Krylov iteration by 40 %. As a result we obtained a memory-efficent FFT-based method with a convergence rate proportional to $\sqrt{\text{cond}}$ whereas the FFT-based method proposed by Lahellec, Moulinec, and Suquet [25] has a convergence rate proportional to the material contrast κ. Furthermore, we discussed the choice of reference material ensuring fastest convergence (Sect. 3) and proposed a memory-minimal convergence criterion. Clearly, our idea for reducing the memory need of the CG method can also be applied in the context of small deformations [48] and to the Lippmann–Schwinger equation for the problem of electric conductivity or heat transfer [44].

By exhibiting the fixed point scheme of Moulinec and Suquet [30] and the counterpart of Eisenlohr et al. [13] for large deformations as a gradient descent method we could explain the strongly growing iteration number in the vicinity of bifurcations of the solution (Fig. 9) and its overall lack of speed which is compensated by its superior robustness and memory efficiency.

Our analytic solution shows a complex effective constitutive behavior despite the simplicity of the microstructure and constitutive properties. The St. Venant–Kirchhoff laminate exhibits bifurcation of the solution (see Fig. 2). For more complex problems (see Fig. 10) all deformations states studied for the St. Venant–Kirchhoff laminate are expected to occur locally at the fiber-matrix interface. Whether the bifurcation can also be observed for complex microstructures or is even only an artifact of the known inconsistencies of the St. Venant–Kirchhoff ansatz might serve as a point of departure for further investigation.

Both the St. Venant–Kirchhoff laminate as well as the GFRP are perfectly described by the stiffness tensor homogenized by the approach of [16] in the range of small and intermediate deformations. For larger strains it is interesting to note that the effective behavior is not reproduced by a St.Venant–Kirchhoff law with the stiffness tensor determined within an infinitesimal theory (see Figs. 5 and 13). Hence, it can be concluded that the effective elastic behavior of a composite consisting of two St. Venant–Kirchhoff materials is in general not given by a macroscopic St.Venant type constitutive relation. This phenomen justifies the need for simulations of complex microstructures at large strains (e.g. crash simulation), hopefully memory-efficient and highly performing (see FeelMath distributed as part of GeoDict).

Acknowledgments The authors benefited from many fruitful discussions with Heiko Andrä and Andreas Günnel.

7 Green's operator for large deformations in Fourier space

An efficient implementation of the basic scheme (Algorithm 1) needs two main ingredients. A fast implementation of the discrete Fourier transformations as provided for example by the FFTW[6] library [20] and an explicit formula for the Fourier coefficients $\hat{\Gamma}^0$ of Green's operator.

The operators ∇, Div and G^0 are understood in Fourier space via

$$\left[\widehat{\nabla d}(\xi)\right]_{kl} = i\xi_l \hat{d}_k(\xi), \tag{54}$$

$$\left[\widehat{\mathrm{Div} D}(\xi)\right]_k = i\xi_l \hat{D}_{kl}(\xi), \tag{55}$$

$$\left[\widehat{G^0 d}(\xi)\right]_k = \hat{G}^0(\xi)_{kl}\hat{d}_l(\xi), \tag{56}$$

for $k, l = 1, \ldots, d$, where $\xi = 2\pi z/L$, $z \in \mathbb{Z}^d$, denotes a wave vector with the short notation $z/L = (z_1/L_1, \ldots z_d/L_d)$. Therefore, in Fourier space the constitutive Eq. (4) and the equilibrium condition (1) have the form

$$\hat{P}_{kL}(\xi) = i\mathbb{C}^0_{kLmN}\xi_N\hat{u}_m(\xi) + \hat{\tau}_{kL}(\xi), \tag{57}$$

$$i\hat{P}_{kL}(\xi)\xi_L = 0, \tag{58}$$

Eliminating $\hat{P}_{kL}$ yields

$$\mathbb{C}^0_{kLmN}\xi_L\xi_N\hat{u}_m(\xi) = i\hat{\tau}_{kL}(\xi)\xi_L. \tag{59}$$

---

[6] www.fftw.org

Due to the definition of the solution operator G^0 this implies

$$(\hat{G}^0)^{-1}_{km}(\xi) = \mathbb{C}^0_{kLmN}\xi_L\xi_N, \tag{60}$$

$$\hat{u}_m(\xi) = \hat{G}^0_{mk}(\xi) i \hat{\tau}_{kL}\xi_L. \tag{61}$$

Using (9) yields additionally

$$\hat{\Gamma}^0_{kLmN}(\xi) = \xi_L\xi_N\hat{G}^0_{km}(\xi). \tag{62}$$

In the case of an isotropic reference material $\mathbb{C}^0$ with Lamé moduli λ_0 and μ_0, i.e. $\mathbb{C}^0 = \lambda_0 I \otimes I + 2\mu_0\mathbb{I}^S$ or $\mathbb{C}^0_{kLmN} = \lambda_0\delta_{kL}\delta_{mN} + \mu_0(\delta_{km}\delta_{LN} + \delta_{kN}\delta_{Lm})$ for $k, L, m, N = 1, \ldots, d$, the Fourier coefficients $\hat{G}^0$ of the solution operator read (cf. [33])

$$(\hat{G}^0)^{-1}_{km}(\xi) = \lambda_0\delta_{kL}\delta_{mN}\xi_L\xi_N + \mu_0(\delta_{km}\delta_{LN} + \delta_{kN}\delta_{Lm})\xi_L\xi_N, \tag{63}$$

$$(\hat{G}^0)^{-1}(\xi) = (\lambda_0 + \mu_0)\xi \otimes \xi + \mu_0|\xi|^2 I, \tag{64}$$

$$\hat{G}^0(\xi) = \frac{(\lambda_0 + 2\mu_0)|\xi|^2 I - (\lambda_0 + \mu_0)\xi \otimes \xi}{\mu_0(\lambda_0 + 2\mu_0)|\xi|^4}. \tag{65}$$

By applying (62) we arrive at an explicit formula for the Fourier coefficients of the Green's operator

$$\hat{\Gamma}^0(\xi)\hat{\tau} = \frac{\hat{\tau}\xi \otimes \xi}{\mu_0|\xi|^2} - \frac{\lambda_0 + \mu_0}{\mu_0\,(\lambda_0 + 2\mu_0)}\frac{\hat{\tau}\xi \cdot \xi}{|\xi|^4}\xi \otimes \xi, \tag{66}$$

$$\hat{\Gamma}^0_{kLmN}(\xi) = \frac{\delta_{km}\xi_L\xi_N}{\mu_0|\xi|^2} - \frac{\lambda_0 + \mu_0}{\mu_0\,(\lambda_0 + 2\mu_0)}\frac{\xi_k\xi_L\xi_m\xi_N}{|\xi|^4}. \tag{67}$$

Symmetrizing $\hat{\Gamma}^0$ gives the Fourier coefficients of Green's operator for linear elasticity.

If the isotropic reference material $\mathbb{C}^0$ with Lamé moduli λ_0 and μ_0 is not symmetrized (cf. Sects. 3.1 and 3.2.5), i.e. $\mathbb{C}^0 = \lambda_0 I \otimes I + 2\mu_0\mathbb{I}$ or $\mathbb{C}^0_{kLmN} = \lambda_0\delta_{kL}\delta_{mN} + 2\mu_0\delta_{km}\delta_{LN}$ for $k, L, m, N = 1, \ldots, d$, the Fourier coefficients $\hat{G}^0$ of the solution operator read

$$(\hat{G}^0)^{-1}_{km}(\xi) = \lambda_0\delta_{kL}\delta_{mN}\xi_L\xi_N + 2\mu_0\delta_{km}\delta_{LN}\xi_L\xi_N, \tag{68}$$

$$(\hat{G}^0)^{-1}(\xi) = \lambda_0\xi \otimes \xi + 2\mu_0|\xi|^2 I, \tag{69}$$

$$\hat{G}^0(\xi) = \frac{(\lambda_0 + 2\mu_0)|\xi|^2 I - \lambda_0\xi \otimes \xi}{2\mu_0(\lambda_0 + 2\mu_0)|\xi|^4}. \tag{70}$$

By applying (62) we arrive at an explicit formula for the Fourier coefficients of the Green's operator

$$\hat{\Gamma}^0(\xi)\hat{\tau} = \frac{\hat{\tau}\xi \otimes \xi}{2\mu_0|\xi|^2} - \frac{\lambda_0}{2\mu_0\,(\lambda_0 + 2\mu_0)}\frac{\hat{\tau}\xi \cdot \xi}{|\xi|^4}\xi \otimes \xi, \tag{71}$$

$$\hat{\Gamma}^0_{kLmN}(\xi) = \frac{\delta_{km}\xi_L\xi_N}{2\mu_0|\xi|^2} - \frac{\lambda_0}{2\mu_0\,(\lambda_0 + 2\mu_0)}\frac{\xi_k\xi_L\xi_m\xi_N}{|\xi|^4}. \tag{72}$$

References

1. Advani SG, Tucker III, CL (1987) The use of tensors to describe and predict fiber orientation in short fiber composites. J Rheol 31(8), 751–784, doi:10.1122/1.549945. URL http://link.aip.org/link/?JOR/31/751/1
2. Agoras M, Castañeda PP (2012) Multi-scale homogenization of semi-crystalline polymers. Phil Mag 92(8):925–958. doi:10.1080/14786435.2011.637982
3. Axelsson O, Kaporin IE (2000) On the sublinear and superlinear rate of convergence of conjugate gradient methods. Numer Algorithm 25(1–4):1–22. doi:10.1023/A:1016694031362
4. Bertram A, Böhlke T, Šilhavý M (2007) On the rank 1 convexity of stored energy functions of physically linear stress-strain relations. J Elast 86(3):235–243. doi:10.1007/s10659-006-9091-z
5. Boyd JP (1989) Chebyshev and Fourier spectral methods. Springer-Verlag, Berlin
6. Braess D (2007) Finite elements: theory. Fast solvers and applications in solid mechanics. Cambridge University Press, Cambridge
7. Brighi B, Bousselsal M (1995) On the rank-one-convexity domain of the Saint Venant-Kirchhoff stored energy function. Rendiconti del Seminario Matematico della Università di Padova 94, 25–45. URL http://eudml.org/doc/108375
8. Brisard S, Dormieux L (2010) FFT-based methods for the mechanics of composites: A general variational framework. Comput Mater Sci 49(3), 663–671. doi:10.1016/j.commatsci.2010.06.009. URL: http://www.sciencedirect.com/science/article/pii/S0927025610003563
9. Brisard S, Dormieux L (2012) Combining Galerkin approximation techniques with the principle of Hashin and Shtrikman to derive a new FFT-based numerical method for the homogenization of composites. Comput Methods Appl Mech Eng 217–220(0):197–212. doi:10.1016/j.cma.2012.01.003. URL http://www.sciencedirect.com/science/article/pii/S0045782512000059
10. Castañeda PP (1996) Exact second-order estimates for the effective mechanical properties of nonlinear composite materials. J Mech Phys Solids 44(6):827–862
11. Castañeda PP, Suquet P (1998) Nonlinear composites. Adv Appl Mech 34(998):171–302
12. Ciarlet PG (1988) Mathematical elasticity: three-dimensional elasticity, vol I. Elsevier, Amsterdam
13. Eisenlohr P., Diehl, M., Lebensohn, R., Roters, F.: A spectral method solution to crystal elasto-viscoplasticity at finite strains. Int J Plast 46(0), 37–53 (2013). doi:10.1016/j.ijplas.2012.09.012. URL http://www.sciencedirect.com/science/article/pii/S0749641912001428
14. Eyre DJ, Milton GW (1999) A fast numerical scheme for computing the response of composites using grid refinement. Eur Phys J 6(01):41–47
15. Feyel, F., Chaboche, J.L.: FE2 multiscale approach for modelling the elastoviscoplastic behaviour of long fibre sic/ti composite materials. Comput Methods Appl Mech Eng, 183(3–4), 309–330 (2000). doi:10.1016/S0045-7825(99)00224-8. URL http://www.sciencedirect.com/science/article/pii/S0045782599002248
16. Francfort G (1983) Homogenization and linear thermoelasticity. SIAM J Math Anal 14(4):696–708. doi:10.1137/0514053
17. Gélébart, L., Mondon-Cancel, R.: Non-linear extension of FFT-based methods accelerated by conjugate gradients to evaluate the mechanical behavior of composite materials. Comput Mater Sci 77(0), 430–439 (2013). doi:10.1016/j.commatsci.2013.04.046. URL http://www.sciencedirect.com/science/article/pii/S0927025613002188
18. Hestenes MR, Stiefel E (1952) Methods of conjugate gradients for solving linear systems. J Res Nat Bureau Stand 49:409–436

19. Hill R (1972) On constitutive macro-variables for heterogeneous solids at finite strain. Proc R Soc Lond A 326:131–147
20. Johnson SG, Frigo M (2007) A modified split-radix FFT with fewer arithmetic operations. Signal Process IEEE Trans on 55(1): 111–119
21. Kocks UF, Tome CN, Wenk HR (1998) Texture and anisotropy: preferred orientations in polycrystals and their effect on materials properties. Cambridge University Press, Cambridge
22. Krawietz A (1986) Materialtheorie. Springer-Verlag, Berlin
23. Kröner E (1971) Statistical continuum mechanics. Springer, Wien
24. Kröner, E.: Bounds for effective elastic moduli of disordered materials. J Mech Phys Solids 25(2), 137–155 (1977). doi:10.1016/0022-5096(77)90009-6. URL http://www.sciencedirect.com/science/article/pii/0022509677900096
25. Lahellec, N., Michel, J.C., Moulinec, H., Suquet, P.: Analysis of inhomogeneous materials at large strains using fast Fourier transforms. In: C. Miehe (ed.) IUTAM Symposium on computational mechanics of solid materials at large strains, Solid mechanics and its applications, vol. 108, pp. 247–258. Springer, Netherlands (2003). doi:10.1007/978-94-017-0297-3_22. URL http://dx.doi.org/10.1007/978-94-017-0297-3_22
26. Michel JC, Moulinec H, Suquet P (2001) A computational scheme for linear and non-linear composites with arbitrary phase contrast. Int J Numer Methods Eng 52(12):139–160. doi:10.1002/nme.275
27. Milton GW (2002) The theory of composites. Cambridge University Press, Cambridge
28. Monchiet V, Bonnet G (2012) A polarization-based FFT iterative scheme for computing the effective properties of elastic composites with arbitrary contrast. Int J Numer Methods Eng 89(11):1419–1436. doi:10.1002/nme.3295
29. Monchiet, V., Bonnet, G.: Numerical homogenization of nonlinear composites with a polarization-based FFT iterative scheme. Comput Mater Sci 79(0), 276–283 (2013). doi:10.1016/j.commatsci.2013.04.035. URL http://www.sciencedirect.com/science/article/pii/S0927025613002073
30. Moulinec H, Suquet P (1994) A fast numerical method for computing the linear and nonlinear mechanical properties of composites. Comptes Rendus de l'Académie des Sciences. Série II, Mécanique, Physique, Chimie, Astronomie 318(11):1417–1423
31. Moulinec H, Suquet P (1998) A numerical method for computing the overall response of nonlinear composites with complex microstructure. Comput Methods Appl Mech Eng 157(1–2):69–94. doi:10.1016/s0045-7825(97)00218-1
32. Moulinec, H., Suquet, P.: Comparison of FFT-based methods for computing the response of composites with highly contrasted mechanical properties. Physica B: Condens Matter 338(1–4), 58–60 (2003). doi:10.1016/S0921-4526(03)00459-9. URL http://www.sciencedirect.com/science/article/pii/S0921452603004599. Proceedings of the Sixth International Conference on Electrical Transport and Optical Properties of Inhomogeneous Media
33. Mura T (1987) Micromechanics of defects in solids. Mechanics of elastic and inelastic solids, 2nd edn. Martinus Nijhoff Publishers, Dordrecht
34. Nemat-Nasser S (1993) Micromechanics: overall properties of heterogeneous materials, North-Holland series in applied mathematics and mechanics. Elsevier Science Publishers B.V, Amsterdam
35. Ortega JM (1968) The Newton-Kantorovich theorem. Am Math Mon 75(6):658–660. doi:10.2307/2313800
36. Ortega JM, Rheinboldt W (1970) Iterative solution of nonlinear equations in several variables. Academic Press, New York
37. Paige CC, Saunders MA (1975) Solution of sparse indefinite systems of linear equations. SIAM J Numer Anal 12(4):617–629. doi:10.1137/0712047
38. Schladitz K, Peters S, Reinel-Bitzer D, Wiegmann A, Ohser J (2006) Design of acoustic trim based on geometric modeling and flow simulation for non-woven. Comput Mater Sci 38(1), 56–66. doi:10.1016/j.commatsci.2006.01.018. URL http://www.sciencedirect.com/science/article/pii/S092702560600019X
39. Schneider M (2014) Convergence of FFT-based homogenization for strongly heterogeneous media. Mathematical methods in the applied sciences n/a(n/a), n/a-n/a. doi:10.1002/mma.3259. URL http://dx.doi.org/10.1002/mma.3259
40. Šilhavý M (1997) The mechanics and thermodynamics of continuous media. Springer, New York
41. Smit RJM, Brekelmans WAM, Meijer HEH (1998) Prediction of the mechanical behavior of nonlinear heterogeneous systems by multi-level finite element modeling. Comput Methods Appl Mech Eng 155(1–2):181–192. doi:10.1016/S0045-7825(97)00139-4. URL http://www.sciencedirect.com/science/article/pii/S0045782597001394
42. Spahn J, Andrä H, Kabel M, Müller R (2014) A multiscale approach for modeling progressive damage of composite materials using fast Fourier transforms. Compu Methods Appl Mech Eng 268(0):871–883. doi:10.1016/j.cma.2013.10.017. URL http://www.sciencedirect.com/science/article/pii/S0045782513002697
43. Truesdell C, Noll W (1965). The non-linear field theories of mechanics, encyclopedia of physics, vol. III. Springer URL http://books.google.de/books?id=dp84F_odrBQC
44. Vinogradov V, Milton GW (2008) An accelerated FFT algorithm for thermoelastic and non-linear composites. Int J Numer Methods Eng 76(11):1678–1695. doi:10.1002/nme.2375
45. Vondrejc J, Zeman J, Marek I (2011) Analysis of a fast Fourier transform based method for modeling of heterogeneous materials. In: Lirkov I, Margenov S, Wasniewski J (eds) LSSC Lecture Notes Computer Science. Springer, Berlin, pp 515–522. doi:10.1007/978-3-642-29843-1_58
46. Vondřejc J (2013) FFT-based method for homogenization of periodic media: theory and applications. Ph.D. thesis, Department of Mechanics, Faculty of Civil Engineering, Czech Technical University, Czech Republic, Prague (2013).
47. Zeller R, Dederichs PH (1973) Elastic constants of polycrystals. Physica Status Solidi (b) 55(2):831–842. doi:10.1002/pssb.2220550241
48. Zeman J, Vondřejc J, Novák J, Marek I (2010) Accelerating a FFT-based solver for numerical homogenization of periodic media by conjugate gradients. J Comput Phys 229:8065–8071. doi:10.1016/j.jcp.2010.07.010. URL http://www.sciencedirect.com/science/article/pii/S0021999110003931